Journal of Magnetic Resonance 235 (2013) 42–49

Contents lists available at ScienceDirect

Journal of Magnetic Resonance

journal homepage: www.elsevier.com/locate/jmr

High-resolution MRI velocimetry compared with numerical simulations

Daniel Edelhoff[a,*], Lars Walczak[b], Stefan Henning[a], Frank Weichert[b], Dieter Suter[a]

[a] Experimental Physics III, TU Dortmund University, Otto-Hahn-Str. 4, 44227 Dortmund, Germany
[b] Computer Science VII, TU Dortmund University, Otto-Hahn-Str. 16, 44227 Dortmund, Germany

ARTICLE INFO

Article history:
Received 23 May 2013
Revised 1 July 2013
Available online 13 July 2013

Keywords:
MRI
Phase contrast
Fluid flow
Computational fluid dynamics
Pipe flow

ABSTRACT

Alterations of the blood flow are associated with various cardiovascular diseases. Precise knowledge of the velocity distribution is therefore important for understanding these diseases and predicting the effect of different medical intervention schemes. The goal of this work is to estimate the precision with which the velocity field can be measured and predicted by studying two simple model geometries with NMR micro imaging and computational fluid dynamics. For these initial experiments, we use water as an ideal test medium. The phantoms consist of tubes simulating a straight blood vessel and a step between two tubes of different diameters, which can be seen as a minimal model of the situation behind a stenosis. For both models, we compare the experimental data with the numerical prediction, using the experimental boundary conditions. For the simpler model, we also compare the data to the analytical solution. As an additional validation, we determine the divergence of the velocity field and verify that it vanishes within the experimental uncertainties. We discuss the resulting precision of the simulation and the outlook for extending this approach to the analysis of specific cases of arteriovascular problems.

1. Introduction

Phase contrast magnetic resonance imaging (PC-MRI) was developed in the early 1980s by [1] and is now an established noninvasive method for measuring fluid flow *in vivo* as well as *in vitro* [2,3]. The technique is used in technical and medical applications where noninvasiveness as well as high spatial resolution is required [4–6]. Many technical developments, including higher magnetic fields and gradient strengths, have improved the signal to noise ratio and allow higher spatial resolution [7–9].

Computational fluid dynamics (CFD) simulations are gaining acceptance for studying biomedical flows, since they provide a relatively effortless access to different fluid models and geometries compared to the process of model building and measuring. At the same time, validation of the simulation results remains a challenge for realistic flows in non-trivial geometries in three dimensions. Experimentally acquired velocities of flowing liquids within different sample geometries for medical purposes have been compared to CFD simulations in earlier studies [10–14]. However, most studies show limitations, like restrictions to symmetric geometries, comparisons with non-3D CFD or low spatial imaging resolutions. Microscopic measurements of velocity vector fields in different geometries can help optimizing the parameters for realistic CFD simulations and providing flow information on complex geometries, which can be compared to the optimized simulations. PC-MRI measurements are also not free from measurement artifacts, such as phase accumulation from higher order moments of the gradients, velocity averaging in a recorded slice, spin flow-out of a slice or susceptibility differences between fluid and wall [15]. Additionally, impurities in the fluid, asymmetries in the experimental setup, unknown temperature influences or other aspects can degrade the measurements. Accordingly, a detailed comparison of high-resolution experimental and numerical data is important for validating both types of data.

Blood is a non-Newtonian fluid, and its flow in human arteries is pulsatile. However, in the present study, which aims at testing the precision limits for the determination of microscopic velocity patterns, we exclude these aspects and concentrate on a Newtonian fluid under conditions of constant flow. This also avoids complications of safety and ethical issues when dealing with (human) blood. As an additional verification tool, we compare the data to analytical solutions and verify that they do not violate known conservation laws.

2. Methods

2.1. Phase contrast MRI

One possible technique for measuring the velocity of moving nuclear spins in a spatially resolved way is PC-MRI [16–18]. Fig. 1 shows the pulse sequence of gradient- and RF-pulses for phase contrast measurements in two-dimensional slices perpendicular to the main flow direction. After the velocity-compensated

---

* Corresponding author.
E-mail address: daniel.edelhoff@tu-dortmund.de (D. Edelhoff).

1090-7807/$ - see front matter © 2013 Elsevier Inc. All rights reserved.
http://dx.doi.org/10.1016/j.jmr.2013.07.002

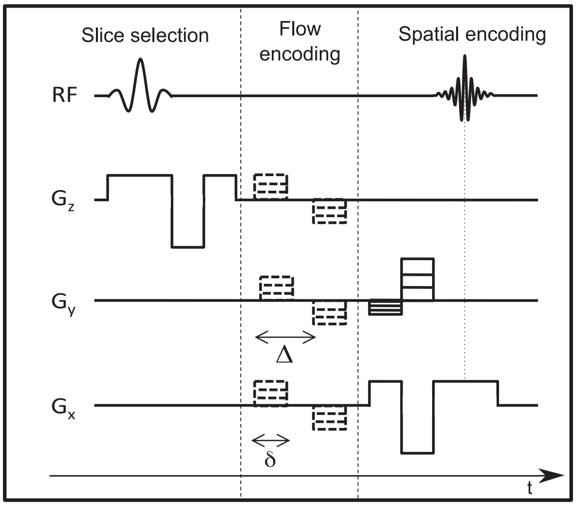

Fig. 1. Schematic representation of the flow encoding imaging sequence. The spatial encoding gradient pulses (solid lines) are flow-compensated. The dashed lines represent the flow encoding.

slice selection (z-direction), a flow-encoding sequence is applied in one of the three orthogonal directions. The spatial encoding and detection part is based on the 'fast low angle shot' (FLASH) technique [19]. It uses flow compensated spatial encoding in the phase- and frequency-encoding direction (y and x in our example), which results in vanishing precession angles for all spins (stationary or with constant velocity) at the time of the echo, in the absence of flow-encoding gradients [17,16].

For non-zero flow-encoding gradients, the phase shift of the spins moving with constant velocity $\mathbf{v} = (v_x, v_y, v_z)$ is

$$\Phi = \gamma v_\alpha G_\alpha \delta \Delta, \quad \alpha = x, y, z. \tag{1}$$

Here, γ is the gyromagnetic ratio, δ and Δ represent the duration of the flow-encoding gradient pulses and the separation between the pulses, respectively, as shown in Fig. 1, and $\mathbf{G}$ is the amplitude of the flow encoding gradient pulses. For each cartesian component, we recorded images with three different gradients (−0.2, 0, and 0.4 T/m). From these images, we calculated the components of the flow velocities by a linear least squares fit of Eq. (1) to the experimental data.

The flow-compensation is realized by optimizing the imaging gradient pulses such that the phase

$$\Phi = \gamma \left(m_0 x + m_1 \frac{dx}{dt} + \frac{m_2}{2} \frac{d^2x}{dt^2} + \cdots \right) \tag{2}$$

vanishes. Here m_n is the nth magnetic gradient moment over the echo time T_e (time from the slice selection to the echo, set to 15 ms),

$$m_n = \int_0^{T_e} G(t) t^n \, dt. \tag{3}$$

The imaging gradients of the shown sequence nullify the gradient moment m_1 and therefore the resulting phase vanishes for spins with constant velocities.

2.2. Computational method

In continuum mechanics (i.e. small Knudsen number flows), the fluid is described by time-dependent velocity-, pressure- and density-fields, which corresponds to a macroscopic point of view. A microscopic point of view on the other hand would be to describe the motion of each fluid molecule. The Lattice Boltzmann method (LBM) takes a third and probabilistic approach, derived from statistical physics, that is positioned in between the two and hence is called mesoscopic. LBM is a relatively new and popular method in CFD and has been applied to a number of interesting flow problems including multi-phase and multi-component fluid flows [20–25]. In LBM, the (macroscopic) density ρ of a fluid is represented by particle distribution functions (PDF) f_i. The larger f_i, the more particles move into the direction $\mathbf{e}_i$ associated with f_i. A common model in three dimensions is $D3Q19$, which considers 19 discrete directions $\mathbf{e}_0 = (0,0,0)$, $\mathbf{e}_{\{1,\ldots,6\}} = \{(\pm c,0,0),\ (0,\pm c,0),\ (0,0,\pm c)\}$, $\mathbf{e}_{\{7,\ldots,18\}} = \{(\pm c,\pm c,0),\ (\pm c,0,\pm c),\ (0,\pm c,\pm c)\}$. The direction $\mathbf{e}_0$ represents particles at rest. The scalar value $c = \delta x/\delta t$ denotes the lattice speed where δx, δt are grid and time steps. To model the viscosity of a fluid, collisions between the moving particles are evaluated during the time evolution. It holds for $i = 0, \ldots, 18$:

$$f_i(\mathbf{x} + \mathbf{e}_i \delta t, t + \delta t) - f_i(\mathbf{x}, t) = -\frac{f_i(\mathbf{x}, t) - f_i^{eq}(\rho, \mathbf{u})}{\tau} \tag{4}$$

in which

$$f_i^{eq}(\rho, \mathbf{u}) = w_i \rho \left(1 + \frac{3(\mathbf{e}_i \cdot \mathbf{u})}{c^2} + \frac{9(\mathbf{e}_i \cdot \mathbf{u})^2}{2c^4} - \frac{3\mathbf{u}^2}{2c^2} \right) \tag{5}$$

are the 19 equilibrium distribution functions and $w_0 = \frac{1}{3}, w_{\{1,\ldots,6\}} = \frac{1}{18}, w_{\{7,\ldots,18\}} = \frac{1}{36}$ are weighting factors for $D3Q19$. The equilibrium distribution functions f_i^{eq} have the property to conserve mass. The term on the right hand side of Eq. (4) is usually referred to as the collision operator. It can be modified to include multiple relaxation times or to model different macroscopic equations. The evolution of the directional densities can be understood as a relaxation towards local equilibrium which is a function of the local density ρ, the current velocity $\mathbf{u}$ and the single relaxation time τ which is connected to the kinematic viscosity

$$\nu = \frac{1}{3} \left(\tau - \frac{1}{2} \right) \frac{\delta x^2}{\delta t}. \tag{6}$$

The density $\rho(\mathbf{x}) = \sum_{i=0}^{18} f_i(\mathbf{x})$ at a lattice node is the sum of all PDFs. Pressure $p = c_s^2 \rho$ is proportional to the density; c_s is the speed of sound of the chosen discretization (e.g. for $D3Q19$ $c_s = \frac{c}{\sqrt{3}}$). The current velocity $\mathbf{u}(\mathbf{x}) = \frac{1}{\rho(\mathbf{x})} \sum_{i=0}^{18} f_i(\mathbf{x}) \cdot \mathbf{e}_i$ is also computed from the PDFs.

Solid boundaries and the no-slip condition can be incorporated by swapping opposite PDFs at solid nodes, this technique is known as bounce-back. To locate the position of the boundaries in the $D3Q19$ grid, the zero isocontour of a level set [26] representing the geometry and defined on the same grid dimensions is used. Steady flow is initiated by setting the velocity distribution at the inlet (Dirichlet conditions) and requiring that the velocity at the outlet is stationary (Neumann conditions). Those boundary conditions [27] are applied on a macroscopic level (e.g. setting $\mathbf{u}$ or ρ to a certain value) as well as on a microscopic level (e.g. depending on the boundary velocity $\mathbf{u}$ one has to set ρ and some of the f_i that point into the fluid). External forces like gravity can be included by manipulating the collision operator and the equilibrium velocity after the collision [28].

2.3. Parametrization of LBM systems to physical reference values

Basic comparisons of LBM with analytic solutions, the analysis of different boundary conditions, forcing terms and other numerical methods like Finite Elements have been done [27,29,28,30–32], but the results are not exhaustive – especially for arbitrary geometries and real flow problems. It has been shown that LBM approximates the time-dependent Navier–Stokes equations under certain circumstances [33]. The choice of the simulation parameters can limit the stability of the method, especially when additional constraints must be considered. Lattice Boltzmann techniques are popular because fast execution times can be achieved by using new programming paradigms for massively parallel processors like graphics processing units (GPUs) available in most workstations [34], but the limited amount of graphics memory can limit the size and the resolution of a full 3D domain and therefore the parameter set. One aspect of this paper is to analyze how the parametrization on the GPU affects the accuracy of the method in comparison with basic analytic solutions and microscopic phase contrast measurements in simple, but asymmetric geometries.

In order to compare MRI measurements and simulation results, the LBM has to be parameterized by transferring the physical quantities and units into their LBM equivalent. Usually a flow is characterized by its Reynolds number

$$Re = \frac{c_U c_L}{\nu} = \frac{c_L^2}{c_T \nu}. \tag{7}$$

In Eq. (7), $c_{\{U,L,T\}}$ are the characteristic velocity, length and time of the flow and ν is the kinematic viscosity of the fluid. A parametrization of LBM has to refer to the same Reynolds number as the physical system, therefore LBM parameters like u_{LBM}, δx, δt, ν_{LBM}, τ and the grid resolution N have to be determined (the first four parameters correspond to $c_{\{U,L,T\}}$, ν). Additionally, Eq. (6) has to be fulfilled, with $\tau > \frac{1}{2}$ for physically meaningful results. Moreover, the compressibility error of the method depends on the Mach number. With a Mach number $Ma = \frac{u_{LBM} c}{c_s} \ll 1$, the simulated liquid is almost incompressible. With these constraints, u_{LBM} has to be as low as possible according to Ma. The parameter for the grid resolution N is set based on the available memory resources, in this case the amount of graphics memory, and the relation

$$N > \sqrt{\frac{Re}{Ma}}, \tag{8}$$

which estimates the maximum kinetically resolved Reynolds number for the grid [35]. With these two parameters, one can calculate $\delta x = \frac{c_L}{N}$ and $\delta t = \frac{u_{LBM} \delta x}{c_U}$. τ is set according to Eq. (6). The gravitational force acting on the fluid can be calculated as well: $f_g = \frac{8 \rho \nu_{LBM}^2}{N^3} Re$.

3. Experimental setup and parameters

For an initial comparison between experimental measurements and simulation results, two simple geometries were chosen. The first consists of a polyvinyl chloride (PVC) tube with a diameter of 6 mm, while the second acts as a minimal model of an artery following a stenosis. We combined two tubes with different diameters of 3 mm and 6 mm resulting in a step. The flow was oriented upwards, from the narrower to the wider section. We also measured the inflow into the stenosis, where we found the expected convective acceleration, but here we discuss only the results from the outflow behind the stenosis, which shows a significantly more interesting flow pattern. The average flow velocity within the measured systems corresponds to typical Reynolds numbers of human arteries [36].

3.1. Experimental setup

The MRI measurements were performed in a 14.1 T wide bore magnet with a gradient unit providing a gradient strength of up to 1 T/m. We used a home-built probe with a 10 mm RF-insert. Fig. 2 shows a summary of the experimental setup. Distilled water with a temperature of 20 °C was used and the hydrostatic pressure from a reservoir above the magnet provided the flow, which was monitored by an inductive flow measurement device. The flow was constant during a measurement period of up to 20 h. During the measurements the water-level in the upper basin was kept constant by a circulation pump. PVC tubes were used as connections between all parts and the samples were placed in the RF-insert.

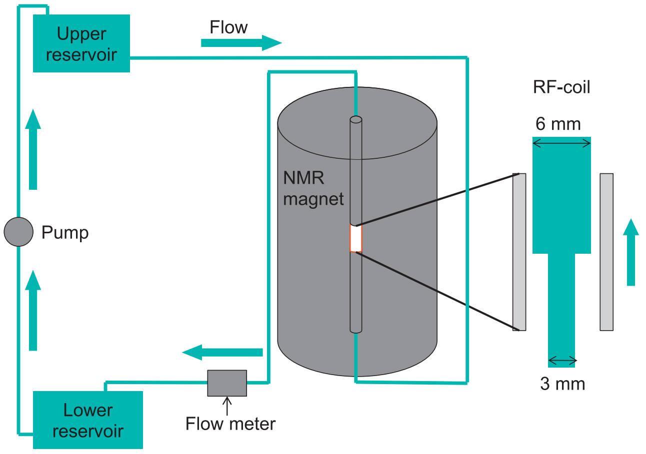

Fig. 2. Schematic representation of the experimental setup.

3.2. Sample geometry

The distribution of flow velocities over a total volume of $7 \times 7 \times 12.3$ mm^3 was measured by acquiring 41 planar phase contrast images within the RF-coil volume ($10 \times 10 \times 15.4$ mm^3). The slices were perpendicular to the main flow direction (z), their thickness was 300 μm, and the spatial resolution within each slice was 27 × 27 μm^2. In the following sections we number the slices from 1 to 41 with increasing z-coordinate. The flow encoding parameters defined in Section 2.1 were $\delta = 1$ ms, $\Delta = 2$ ms, $G_{(x,y,z)} = -0.2$, 0 and 0.4 T/m. We used the maximum slew rate of the system, which is $\approx 1.2 \times 10^4$ T m^{-1} s^{-1}. This results in a phase shift of π (known as VENC) for a velocity of 8.8 cm/s, which fits the experimental z components of the velocity.

The reference images, without flow encoding gradients, were also used to generate a three dimensional image of the geometry. Fig. 3 shows the reconstructed geometries for both systems. These data were used as boundary conditions for the LBM simulations.

The data showed that the cross section of the tubes could be well represented by ellipses. This allowed us to compare the measured flow patterns to an analytical solution which exists for elliptical boundaries. For this comparison, we determined the parameters of the elliptical boundary in every slice individually. The centers of the ellipses were used to determine the precise orientation of the tube axis. Averaged over the straight tube, the major and minor semi-axes were $a = 3.054$ mm and $b = 2.866$ mm, which corresponded to an ellipticity of 7.6%. Comparing the centers

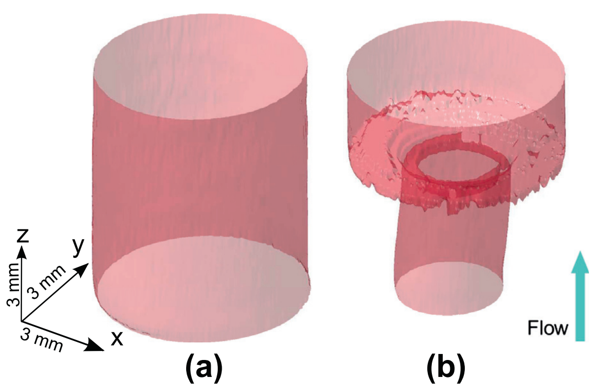

Fig. 3. Geometries of the samples reconstructed from the MRI data. (a) 6 mm diameter PVC tube and (b) 3–6 mm step model. The flow is orientated in the positive z-direction and the length of the axes corresponds to 3 mm.

of the ellipses, we determined that the tube was inclined by ≈1° in the x-direction and ≈0.5° in the y-direction. The orientation of all ellipses was constant (≈8°).

In the step model, we determined these characteristics separately for the part near the entrance (3 mm diameter) and the wider part near the exit (6 mm). Within the narrower part, the major and minor axes were $a = 1.539$ mm and $b = 1.458$ mm, which corresponds to an ellipticity of 2.7%. The orientation the ellipses in the wider part changed from ≈6° in slice 1 to ≈18° in slice 25. The axis of this phantom was inclined by 1.5° in the x-direction and 2.1° in the y-direction. The inclination of the wider part was smaller (0.3° in both directions). The ellipticity was 1.5% with the major and minor axes $a = 2.943$ mm and $b = 2.916$ mm. Here, the orientation of all ellipses was constant, at ≈0°.

3.3. LBM parameters

The simulation domain was obtained by a level set reconstruction [37] of the measured MRI geometry. The simulations were set up according to PC-MRI velocity measurements and the fluid used in the experiment (distilled water at 20 °C, density $\rho = 998.21$ kg/m^3, dynamic viscosity $\eta = 1.002$ g/ms). The first PC-MRI slice was used as inflow boundary condition while the maximum velocity of the slice v_0 (see Eq. (9) in Section 4.5) was selected for setting the characteristic velocity $u_C = \frac{1}{2}v_0$. For flow through the straight tube, the resulting key parameters were $Re = 147.43$, $u_{LBM} = 0.07$, $N = \{57, 85, 113, 140, 169\}$ ($u_L = 6$ mm). The different values for Ns were chosen for convergence analysis. Regarding the flow through the step model from 3 mm to 6 mm, the resulting numbers were $Re = 192.98$, $u_{LBM} = 0.07$, $N = 86$ ($u_L = 3$ mm). Relation (8) was satisfied for all N. All other parameters mentioned in Section 2.3 were inferred based on these values.

4. Results

4.1. Flow distribution in the straight tube

We measured the microscopic flow distribution for each slice and both geometries within the tubes. The straight tube showed a Hagen–Poiseuille distribution, as expected [38,39]. The mean flow velocity was $\bar{v}_z = (3.13 \pm 1.79)$ cm/s, while the perpendicular components were of the order of $\bar{v}_\perp = (0.16 \pm 0.09)$ cm/s. Fig. 4 shows the measured flow distribution. The left hand side shows the centered x–z-plane. The in-plane components of the velocity are visualized by vectors. Additionally the z-component is color encoded to point out the main flow behavior. The z-component was processed with a 3 × 3 pixel median filter to reduce the noise. The right hand side shows the measured slice No. 12, 3.6 mm from the bottom, while the upper part shows the flow profile through the indicated line. It shows the expected parabolic shape, with the maximum velocity close to the center of the ellipses, with a deviation of 54 μm. The maximum velocity was $v_{max} = (6.3 \pm 0.2)$ cm/s.

4.2. Flow distribution in the minimal step model

The flow in the step model is more complex than in the straight tube. In the lower part we observed again a parabolic distribution of the flow velocity, as expected for a Hagen–Poiseuille flow. At the step, the pattern becomes wider and in the outer parts, we observed flow in the direction opposite to the main flow, indicating the formation of a vortex.

Fig. 5 plot the flow distribution in different sections of the complete vector field. The left hand part of the figure shows one x–z-plane. The color scheme indicates the backward flow behind the transition. The narrower section is inclined by 2.1° from the z-axis. The right hand side of the figure shows the vector field in the inflowing plane (lower graph) as well as the outflowing plane (upper graph). The velocity components follow the inclination of the geometry, which results in a shift of the flow distribution in the wider part, as expected from momentum conservation. Additionally the negative flow decreases with increasing distance from the step, and the flow profile becomes wider. This indicates that the backward flow disappears with increasing distance from the step and the in-plane distribution approaches the normal parabolic shape. The mean flow velocity at the inlet was $\bar{v}_{zin} = 6.08 \pm 3.88$ cm/s, and in the wider part it was reduced to $\bar{v}_{z\ out} = 1.51 \pm 2.25$ cm/s, with a perpendicular component of $\bar{v}_\perp = 0.17 \pm 0.12$ cm/s.

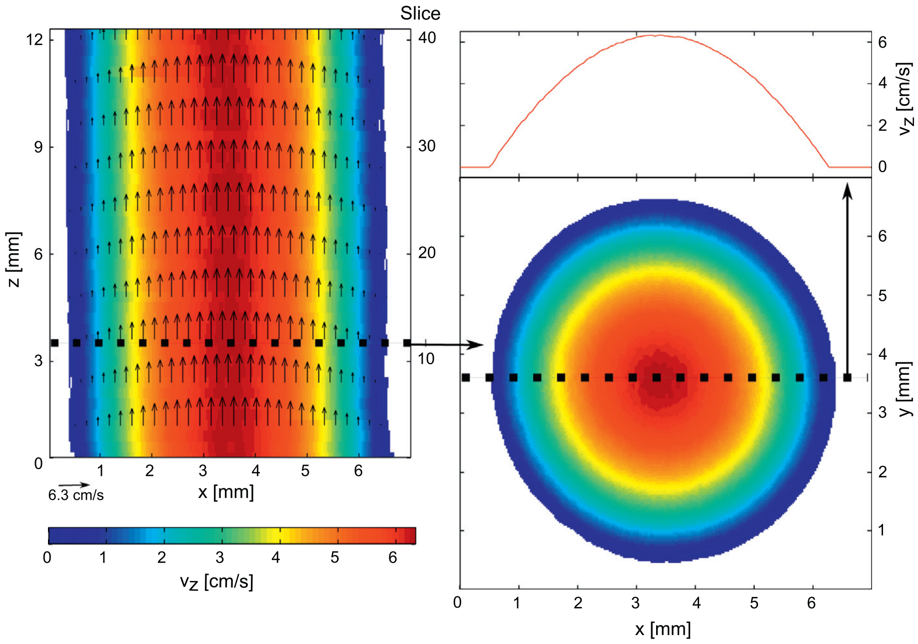

Fig. 4. Measured flow distribution of the straight tube in different perspectives. The left hand side shows one x–z-plane of the vector field, while the right hand side shows the z-component of slice No. 12. The upper graph is the flow profile through the center of the lower slice.

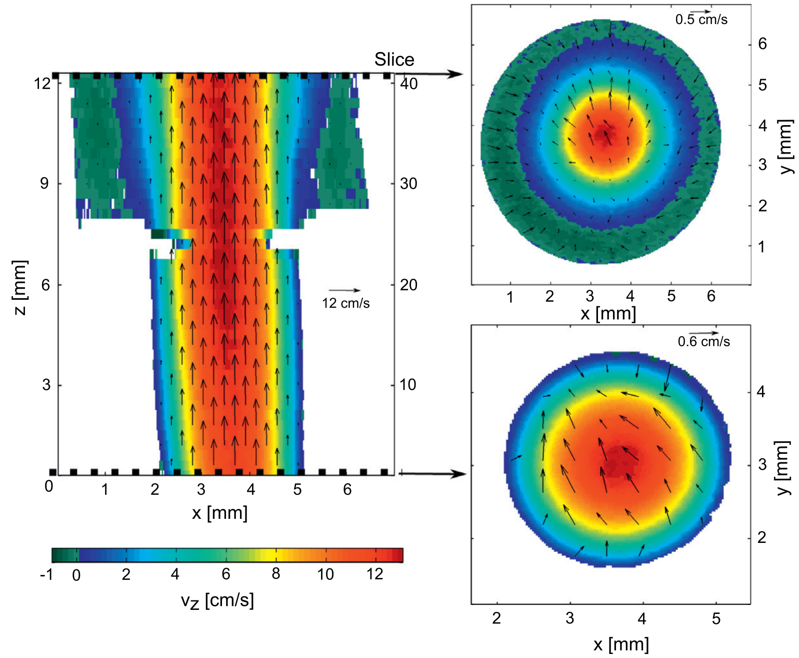

Fig. 5. Measured flow distribution of the step model in different perspectives. The left hand side shows the central *x*–*z*-plane of the vector field, while on the right hand side the inflowing as well as the outflowing slice is shown.

4.3. Validation

To validate these results, we used three independent checks: For the straight tube, we compared the measured data to the analytical solution. For both geometries, we calculated the divergence $\nabla \cdot \mathbf{v}$ (mass conservation) and compared the measured distribution to the numerical solutions. The analytical solution for the straight tube uses the measured elliptical cross section to determine the *z*-component of the velocity, while the perpendicular components vanish. For the usual no-slip boundary conditions, the solution is

$$v_z(x,y) = v_0 \cdot \left(1 - \frac{x^2}{a^2} - \frac{y^2}{b^2}\right), \tag{9}$$

[40] where *a* and *b* are the semi-major and -minor axis determined in Section 3.2.

Fig. 6(a and b) shows the measured flow profile along the determined major and minor axis of the ellipse from slice No. 12 of the straight tube. A comparison shows good results with small deviations of less than 1% in the center, relative to the maximum velocity. At the boundary, the finite precision with which the ellipsis was determined, resulted in deviations up to 2.5%. Fig. 6(c) shows the deviation over the complete slice. In the straight tube, the average deviation was 1.15 ± 0.96% which is mainly due to the in-plane velocities, which were not considered, and noise and inaccuracies in the fitting process of the ellipses.

For both geometries, we calculated the divergence of the experimentally determined velocity field, which should vanish for an incompressible fluid. The divergence was calculated as

$$\nabla \cdot \mathbf{v} = \frac{\delta v_x}{\delta x} + \frac{\delta v_y}{\delta y} + \frac{\delta v_z}{\delta z}. \tag{10}$$

Due to the non-cubic dimensions of the voxels ($27 \times 27 \times 300\ \mu\text{m}^3$), the variations of the in-plane components had a higher influence to the determined divergence. The mean value of the divergence was $0.0046 \pm 14.86\ \text{s}^{-1}$ for the straight tube and $0.27 \pm 4.49\ \text{s}^{-1}$ for the step model. These values are well compatible with zero and are mostly due to the noise of the *x*–*y*-velocity components. No systematic trend was observed, except for a slightly increased divergence near the tube wall. The signal to noise ratio (SNR) in the measured images was ≈20 and due to the used velocity phase encoding (VENC) we could estimate the standard deviation σ of the determined velocities as [41]:

$$\sigma = \frac{\sqrt{2}}{\pi}\frac{\text{VENC}}{\text{SNR}}. \tag{11}$$

We determined σ to 0.2 cm/s and therefore the measured in-plane velocities were of the same order as the noise.

4.4. Numerical results

In the straight tube case, the simulations were performed with different lattice resolutions to analyze the convergence behavior. We used the first measured slice as the inflow condition for the simulation and the measured geometry for the bounce-back boundary condition. The in-plane lattice resolution in pixel (px) of the simulation was varied for the straight tube experiment between 64 and 192 px to simulate the measured 7 mm field of view, while the *z*-axis was simulated in a higher resolution than the measurement (41 slices) to achieve equidistant step sizes within the simulation. The *z*-axis resolution varied between 124 and 368 px. The highest possible resolution was limited by the amount of memory on the GPU. Fig. 7 shows the absolute deviation of the measured and simulated *z*-velocities for the measured geometry referred to the maximum *z*-velocity of the measurement.

The deviation between the simulated and experimental values of the in-plane components was 2.4 ± 4.4%, independent of the lattice resolution. These values are compatible with zero and can be well explained by the noise of the experimental data, which is of the order of 3% of the maximum velocity (see Section 4.3).

The figure shows that with increasing lattice resolution the deviation decreases to a minimum value of 0.75 ± 0.58% and in total shows a quadratic convergence behavior. We validated these values by simulating an ideal tube with different lattice resolutions from 64 to 256 px^3 and compared the results with the well known analytic solution for an ideal tube. These results are shown in Fig. 7 as well. The convergence behavior was the same as in the real

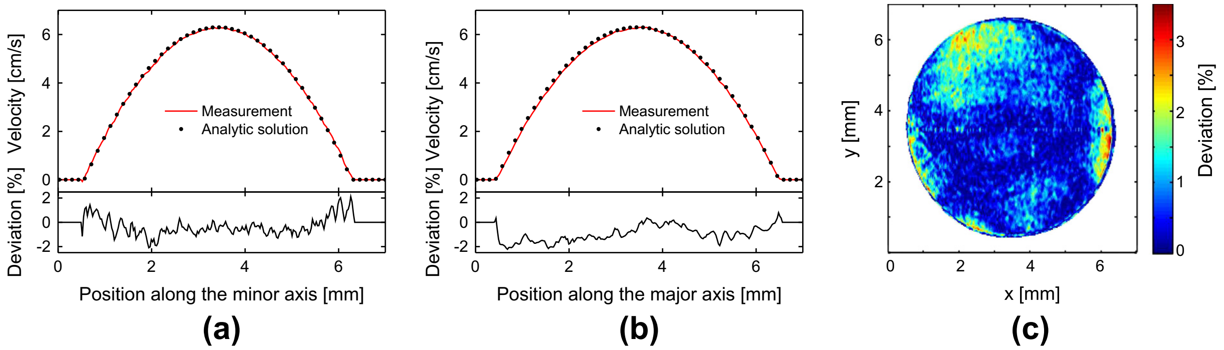

Fig. 6. Measured and calculated velocities along the symmetry axis of the determined ellipses of slice No. 12 in the straight tube. The deviation between analytic solution and measurement is shown as well (a and b). Deviation between measurement and analytic solution in the complete slice No. 12. (c).

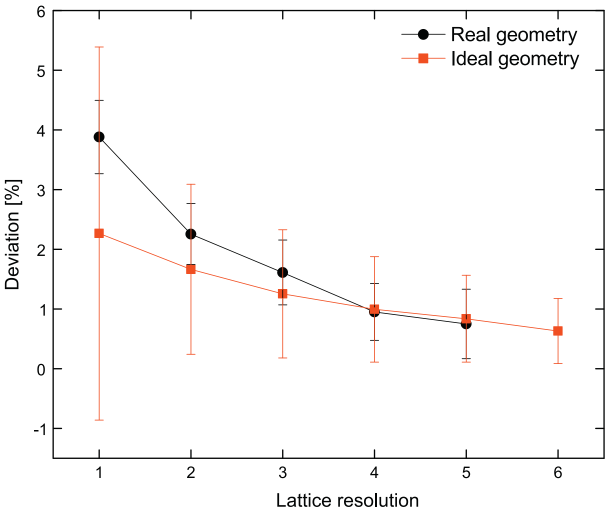

Fig. 7. Absolute deviation between simulated velocities and the analytic solution for the ideal tube geometry as well as measured and simulated flow in the real geometry, relative to the maximum velocity. The *x*-axis shows different in-plane resolutions (1. 64^2 px^2; 2. 96^2 px^2; 3. 128^2 px^2; 4. 160^2 px^2; 5. 192^2 px^2; 6. 256^2 px^2).

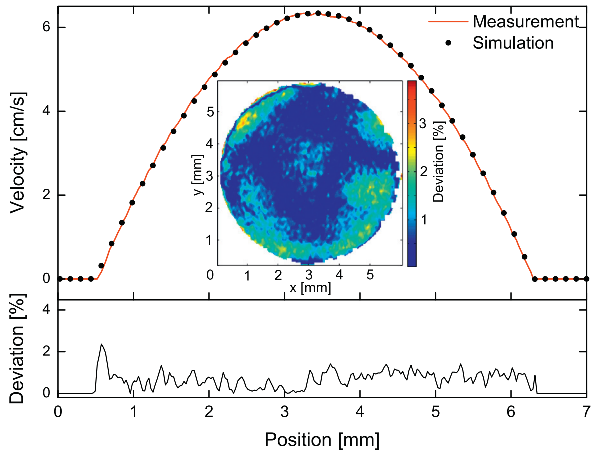

Fig. 8. Simulation and measurement results for the tube setup along the major axis of the ellipses in slice No. 13. The lower part and the slice show the absolute deviation referenced to the maximum velocity.

straight tube and decreases to 0.64 ± 0.62)%. The deviation was mainly caused by the bounce-back boundary condition of the simulation which is reported to be at most of second order accuracy, depending on the geometry and viscosity [29,31]. The divergence of the velocity field in the straight tube simulation was $0.0001 \pm 0.6437\ \mathrm{s}^{-1}$ in the highest resolution, the density differences and therewith the compressibility $\lesssim 1\%$.

Once the convergence had been shown, the simulation of the step model was performed with the highest possible lattice resolution of $192 \times 192 \times 368\ \mathrm{px}^3$. We used the inflowing slice of the measurement as starting condition and the measured geometry for the boundaries. In this resolution, the domain for the transition is approximated by $\approx 13.6 \times 10^6$ *D*3*Q*19 cells of which $\approx 12.5 \times 10^6$ cells represent the fluid. With our OpenCL GPU implementation 32.5 LBM-iterations per second were possible with a single NVIDIA 680GTX graphics card and 4 GB RAM; with simultaneous flow field volume visualization this number drops to 25.9 iterations per second. One second in the given parametrization consists of 26443 LBM time steps and can be simulated in about 14 min.

4.5. Comparison with simulated data: straight tube

Fig. 8 compares the simulated and measured *z*-components of the vector fields along the major axis of the fitted ellipses for slice No. 12 (3.6 mm from the bottom) and also shows the color-coded deviation over the entire slice. The shape of the flow profile is very close to the expected parabola and the deviation between both profiles is, except for the left boundary, of the order of 1% and mainly influenced by measurement uncertainties (e.g. noise). The complete slice shows some uncertainties at the boundary of the tube but at a large range the variation is marginal and the simulation agrees with the measured data. The deviation between measurement and simulation of the complete straight tube was 0.64 ± 0.62%.

4.6. Comparison with simulated data: Step model

Within the step model, we observed a higher mean deviation between measurement and simulation than in the straight tube, but the mean value over the complete geometry is adequate with 2.97 ± 3.49% deviation of the maximum velocity. Fig. 9 shows the deviation as a function of major and minor axis as well as in two different slices (3 and 38) of the smaller and the wider part of the geometry. We observed that in the inflowing part (Fig. 9(c and d)) both, measurement and simulation, showed the expected Hagen–Poiseuille flow behavior. The deviation was of the order of 1 – 4%. Within the wider part (Fig. 9(a and b)), the measured flow distribution differed obviously from the simulated velocities. The maximum velocity was determined at different points (≈270 µm difference) and the velocities differ by up to 25%. While the shape of the velocity distribution agrees very well between the two data sets, they are shifted laterally with respect to each other.

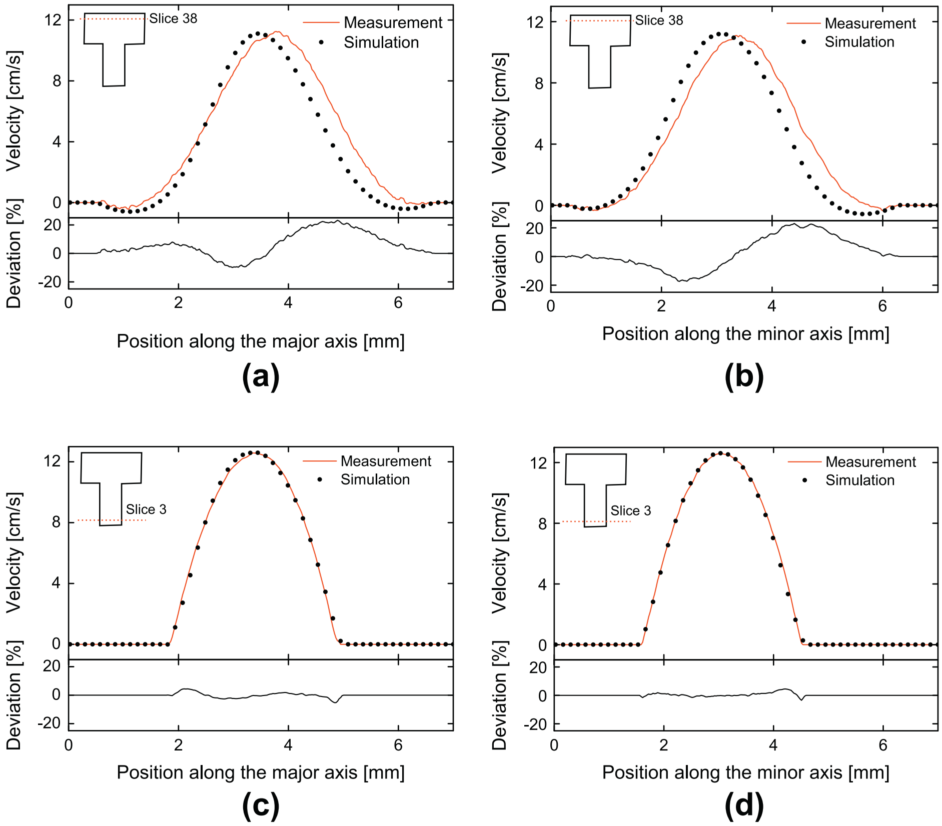

Fig. 9. Measured and simulated velocities along the major and minor axis of the fitted ellipses of different slices and the difference between simulated and measured flow distributions referred to the maximum velocity.

This shift can be explained by the fact that the geometry after the outlet was not simulated. Investigations of the tube system after the RF-coil revealed a slight bend which was not included in the simulation and introduced the shift of the flow. The Neumann boundary condition (see Section 2.2) applied in the simulation could not take this into account. As an alternative, the last measured slice was set as an additional Dirichlet velocity boundary condition at the outlet. The simulation did not show a higher pressure which means that the flow rates at in- and outlet were the same. At the same time, this setup did not lead to an overall lower error in the bulk of 6 mm part of the tube except for the last slices near the outlet where the error vanished because the simulated flow tried to adopt to the Dirichlet condition. Because of this forcing of the flow, the recirculation zones in this simulation setup were different compared to those obtained by the Neumann condition as well as by the measurement.

5. Discussion

Our results show that microscopic PC-MRI gives a very precise picture of flow in the straight tube model. Our computational results, which used the experimental geometry as boundary conditions, achieved good agreement with the measured velocity distribution, with deviations of $\lesssim 1\%$ under physiologically relevant velocity conditions. The main deviations appear near the boundary where both methods, measurement and simulation, are sensitive to artifacts. MRI is influenced by magnetic field inhomogeneities caused by susceptibility differences. On the other hand LBM is largely influenced by the outflow boundary conditions and domain length. The reported accuracy of the bounce-back boundary condition depending on the geometry and viscosity played only a minor role in the results. The convergence of the simulation to the measurement as well as the analytic velocity distribution showed that a large amount of graphics memory is necessary to achieve satisfactory results for microscopic flow distributions.

In the minimal stenosis phantom (step model), the deviations were larger. Here, the initial section showed the same behavior as the straight tube model, with slightly higher deviation and variation, possibly because of the narrower tube (3 mm vs. 6 mm), higher average velocities ($\approx$6 cm/s vs. $\approx$3 cm/s), or the influence of the outflow boundary condition (see below). Behind the transition, measurement and simulation showed a shifted main flow. The symmetry of the deviation, the similarity of the backward flow as well as the identical peak velocity indicate that additional influences affected the flow, which were not accounted for by the simulation. The most likely cause is a bend in the tube outside of the section that was measured and simulated. The Neumann boundary condition seems to be the right choice for the outflow, more suitable than a second Dirichlet condition. The measurement of the velocities close to the transition between the two diameters was influenced by magnetic field inhomogeneities and the resulting inaccuracies within the reconstructed geometry could be another reason for variations between measured and simulated flow data.

For further applications, tube materials with magnetic susceptibilities closer to the sample liquids could be used to avoid and minimize these imaging artifacts. Knowledge of the geometry of the supply tubes outside of the sample volume is necessary to achieve better agreements between measurement and simulation. The simulation could further be improved by using adaptive step sizes to avoid running of out memory resources when simulating more complex systems measured with higher spatial resolution. Clearly, this would significantly increase the complexity of the implementation. Compared to the measurements, the simulation could provide more accurate information of the flow along the slice selection direction of the measurement where the spins are averaged over a rather large slice thickness of 300 μm.

6. Conclusion

Our results show that the PC-MRI measurement procedure is well suited for determining velocity distributions with microscopic resolution under steady flow conditions so that it can be extended for future medical applications were high resolution is required. This will include the analysis of pulsatile flows, non-Newtonian fluid behavior, suspensions and more realistic models of blood vessels. The determined flow distributions agree very well with analytical solutions where they are available. A comparison with CFD simulations also shows a very good agreement. The deviations can be attributed to the finite size of the measured and simulated region of the sample. These differences could thus be eliminated by increasing the region of interest, at the cost of an increased measurement time and higher memory requirements for the simulation. Depending on the available hardware, this leads to limitations in the parametrization, e.g. of the maximum Reynolds number. Alternatively, the setup could be adjusted by changing the part outside the region of interest to sufficiently long rigid straight tubes. However, this approach is not compatible with flow measurements in biological systems like blood vessels, which are not straight. The hardware limitations on the simulation parameters could be reduced by using computer systems with multiple cards working together. Microscopic PC-MRI and CFD simulations may therefore become useful complementary tools for analyzing the flow of non-Newtonian liquids in different medically relevant systems, such as new and optimized endovascular devices.

Acknowledgment

The authors would like to offer their sincerest gratitude to Mercator Research Center Ruhr (MERCUR) for funding this work as part of Project PR-2012-0046.

References

[1] P. Moran, A flow velocity zeugmatographic interlace for NMR imaging in humans, Magn. Reson. Imag. 1 (1982) 197–203.

[2] Y. Xia, Imaging the velocity profiles in tubeless siphon flow by NMR microscopy, J. Magn. Reson. 164 (2003) 365–368.

[3] P. Callaghan, Velocity and diffusion imaging in dynamic NMR microscopy, J. Magn. Reson. 352 (1991) 326–352.

[4] L.F. Gladden, A.J. Sederman, Recent advances in flow MRI, J. Magn. Reson. 229 (2013) 2–11.

[5] K. Packer, Diffusion and flow in fluids, Encyclopedia Magn. Reson. (2007).

[6] K. Romanenko, D. Xiao, B.J. Balcom, Velocity field measurements in sedimentary rock cores by magnetization prepared 3D SPRITE, J. Magn. Reson. 223 (2012) 120–128.

[7] J. Aguayo, S. Blackband, J. Schoeniger, Nuclear magnetic resonance imaging of a single cell, Nature 322 (1986) 190–191.

[8] S. Henning, D. Edelhoff, B. Ernst, S. Leick, H. Rehage, D. Suter, Characterizing permeability and stability of microcapsules for controlled drug delivery by dynamic NMR microscopy, J. Magn. Reson. (2012) 11–18.

[9] J.R. Brown, T.I. Brox, S.J. Vogt, J.D. Seymour, M.L. Skidmore, S.L. Codd, Magnetic resonance diffusion and relaxation characterization of water in the unfrozen vein network in polycrystalline ice and its response to microbial metabolic products, J. Magn. Reson. 225 (2012) 17–24.

[10] P. van Ooij, A. Guédon, C. Poelma, J. Schneiders, M. Rutten, Complex flow patterns in a real-size intracranial aneurysm phantom: phase contrast MRI compared with particle image velocimetry and computational fluid dynamics, NMR Biomed. 25 (2012) 14–26.

[11] I. Marshall, S. Zhao, P. Papathanasopoulou, P. Hoskins, Y. Xu, MRI and CFD studies of pulsatile flow in healthy and stenosed carotid bifurcation models, J. Biomech. 37 (2004) 679–687.

[12] Y. Papaharilaou, D. Doorly, Assessing the accuracy of two-dimensional phase-contrast MRI measurements of complex unsteady flows, J. Magn. Reson. Imag. 723 (2001) 714–723.

[13] I. Marshall, M. Robertson, MRI measurement of wall shear stress vectors in bifurcation models and comparison with CFD predictions, J. Magn. Reson. Imag. 573 (2001) 563–573.

[14] Q. Long, X. Xu, B. Ariff, S. Thom, D. Hughes, V. Stanton, Reconstruction of blood flow patterns in a human carotid bifurcation: a combined CFD and MRI study, J. Magn. Reson. Imag. 11 (2000) 299–311.

[15] K.W. Moser, E.C. Kutter, J.G. Georgiadis, R.O. Buckius, H.D. Morris, J.R. Torczynski, Velocity measurements of flow through a step stenosis using magnetic resonance imaging, Exp. Fluids 29 (2000) 438–447.

[16] J. Pope, S. Yao, Quantitative NMR imaging of flow, Concepts Magn. Reson. 5 (1993) 281–302.

[17] E. Fukushima, Nuclear magnetic resonance as a tool to study flow, Ann. Rev. Fluid Mech. (1999) 95–123.

[18] C.J. Elkins, M.T. Alley, Magnetic resonance velocimetry: applications of magnetic resonance imaging in the measurement of fluid motion, Exp. Fluids 43 (2007) 823–858.

[19] A. Haase, J. Frahm, D. Matthaei, W. Hanicke, K. Merboldt, FLASH imaging. Rapid NMR imaging using low flip-angle pulses, J. Magn. Reson. 67 (1986) 258–266.

[20] Y. Schaefer, Equations of state in a lattice boltzmann model, Phys. Fluids 18 (2006).

[21] M. Sukop, D. Thorne, Lattice Boltzmann Modeling: An Introduction for Geoscientists and Engineers, Springer, Heidelberg,Berlin, New York, 2006.

[22] T. Inamuro, T. Ogata, S. Tajima, N. Konishi, A lattice boltzmann method for incompressible two-phase flows with large density differences, J. Comput. Phys. 198 (2004) 628–644.

[23] S. Succi, The Lattice Boltzmann Equation for Fluid Dynamics and Beyond, Clarendon Press, Oxford University Press, Oxford New York, 2001.

[24] S. Chen, G. Doolen, Lattice Boltzmann method for fluid flows, Ann. Rev. Fluid Mech. 30 (1998) 329–364.

[25] X. Shan, H. Chen, Lattice boltzmann model for simulating flows with multiple phases and components, Phys. Rev. E 47 (1993) 1815–1819.

[26] J. Sethian, Level Set Methods and Dynamic Implicit Surfaces – Evolving Interfaces in Computational Geometry, Fluid Mechanics, Computer Vision, and Materials Science, Cambridge Monographs on Applied and Computational Mathematics, Cambridge University Press, New York, 1999.

[27] Q. Zou, X. He, On pressure and velocity flow boundary conditions for the lattice boltzmann BGK model, Biophysics 9 (1995) 16.

[28] Z. Guo, C. Zheng, B. Shi, Discrete lattice effects on the forcing term in the lattice Boltzmann method, Phys. Rev. E 65 (2002).

[29] X. He, Q. Zou, L.S. Luo, M. Dembo, Analytic solutions of simple flows and analysis of nonslip boundary conditions for the lattice Boltzmann BGK model, J. Statist. Phys. 87 (1997). http://link.springer.com/article/10.1007%2FBF02181482.

[30] S. Geller, M. Krafczyk, J. Tölke, S. Turek, J. Hron, Benchmark computations based on Lattice Boltzmann, finite element and finite volume methods for laminar flows, Comput. Fluids 35 (2006) 888–897.

[31] Z. Yang, Analysis of Lattice Boltzmann Boundary Conditions, Ph.D. thesis, University of Konstanz, Germany, 2007.

[32] F. Weichert, L. Walczak, D. Fisseler, T. Opfermann, M. Razzaq, S. Turek, R. Münster, I. Grunwald, C. Roth, C. Veith, M. Wagner, Simulation of intra-aneurysmal blood flow by using different numerical methods, Comput. Math. Methods Med. (2013), http://dx.doi.org/10.1155/2013/527654.

[33] M. Junk, W.-A. Yong, Rigorous Navier–Stokes limit of the lattice boltzmann equation, Asymptotic Anal. 35 (2003) 165–184.

[34] L. Walczak, D. Fisseler, F. Weichert, Exploring therapy options with an interactive simulation of intra-aneurysmal blood flow on the GPU, GI-Jahrestagung (2012) 1745–1754.

[35] S. Chikatamarla, S. Ansumali, I. Karlin, Grad's approximation for missing data in lattice Boltzmann simulations, Europhys. Lett. 74 (2) (2006) 215–221.

[36] D.N. Ku, Blood flow in arteries, Ann. Rev. Fluid Mech. 29 (1997) 399–434.

[37] L. Walczak, F. Weichert, A. Schröder, C. Landes, H. Müller, M. Wagner, Evaluating the impact of shape on finite element simulations in a medical context, in: Modelling the Physiological Human, Lecture Notes in Computer Science, Springer 5903 (2009) 95–109.

[38] O. Reynolds, An experimental investigation of the circumstances which determine whether the motion of water shall be direct or sinuous, and of the law of resistance in parallel channels, Philos. Trans. Roy. Soc. Lond. 174 (1883) 935–982.

[39] S. Sutera, R. Skalak, The history of Poiseuille's law, Ann. Rev. Fluid Mech. (1993).

[40] L. Landau, E. Lifshitz, Course of Theoretical Physics, vol. 6, Pergamon Press, 1965.

[41] A. Andersen, J. Kirsch, Analysis of noise in phase contrast MR imaging, Med. Phys. (1996).